PAPER

Check for updates

Hierarchical porous $LiNi_{1/3}Co_{1/3}Mn_{1/3}O_2$ with yolk–shell-like architecture as stable cathode material for lithium-ion batteries†

Zhen Chen, [ID] [ab] Dongliang Chao, [ID] [b] Minghua Chen [ID] *[a] and Zexiang Shen [ID] *[b]

The relatively sluggish lithium ion diffusion of $LiNi_{1/3}Co_{1/3}Mn_{1/3}O_2$ (NCM) is one of the fatal factors which can significantly prevent its widespread usage in high-power applications. In this work, the monodispersed hierarchical porous yolk–shell-like $LiNi_{1/3}Co_{1/3}Mn_{1/3}O_2$ (YS-NCM) with exposure to {010} electrochemical active facets was successfully synthesized, aiming to elevate the lithium ion diffusion ability and thus to enhance the electrochemical performance. The hierarchical porous nano-/microsphere morphology as well as the voids between the yolk and the shell allow for shortened Li^+ diffusion pathways, leading to improved Li^+ diffusion capability. These voids are also beneficial for providing more buffers for the volume changes during repeated charge and discharge. Additionally, the exposure of {010} electrochemical active facets provides more open structure for unimpeded Li^+ migration. Therefore, by this design strategy, the lithium ion transport kinetics is greatly improved, yielding superior electrochemical performances. When examined as the cathode material for lithium-ion batteries (LIBs), the YS-NCM-based cells have achieved superior rate capability and stable cycling performance, rendering it as a promising cathode candidate for practical lithium-ion battery applications.

1. Introduction

Over the past decades, impelled by the exhaustion of fossil fuels and the increasingly prominent environmental problems, the significance of developing efficient and green energy storage devices has grown tremendously.[1,2] Lithium-ion batteries (LIBs) featuring high energy density, long cycle life, superior safety and low cost have successfully conquered the market of portable consumer devices, and have been drawing tremendous attention for large-scale applications such as electric vehicles (EVs) and hybrid electric vehicles (HEVs).[3–6] As a derivative of $LiCoO_2$, the symmetrical ternary layered $LiNi_{1/3}Co_{1/3}Mn_{1/3}O_2$ (NCM), which exhibits much higher deliverable capacity with enhanced safety, was firstly reported by Ohzuku and Makimura in 2001.[7–9] This finding later has evoked enormous academic and industrial interest in seeking derivatives with a combination of higher energy density, lower cost, better thermal and structural stability and improved safety properties.[7,8,10–16] However, these targets are difficult to meet at the same time. In fact, recently more and more

interest has been focusing on increasing the nickel content (*i.e.*, Ni-rich NCM), in order to achieve higher capacity and energy density with less cost. Nonetheless, this usually is realized at the cost of not only reduced chemical and structural stability and thus shortened cycling lifetime, but moreover reduced thermal stability and safety as well. These are primarily attributed to (1) more severe Li^+/Ni^{2+} cation mixing that can trigger phase transitions; (2) the formation of surface lithium-containing residuals (*e.g.*, LiOH, Li_2CO_3) that can not only build accumulative resistance hindering the charge transfer at the interface of electrode/electrolyte but also generate gas (O_2, CO, CO_2) during cycling; (3) the formation of oxygen species due to the reactions of highly reactive Ni^{4+} at delithiation status with electrolyte, concomitantly with structural evolutions.[17–19] By far, $LiNi_{1/3}Co_{1/3}Mn_{1/3}O_2$ which shows advantages of better structural and thermal stability and more stable cycling stability over those Ni-rich NCM cathode materials, has been deemed as the most ideal cathode material because of its overall modest performance.[20] However, drawbacks including the fatal capacity degradation in terms of long cycles and inferior rate capability especially at high C-rates as a result of sluggish lithium ions diffusion ($\sim 10^{-11}$ cm^2 s^{-1})[21,22] have impeded its wide spread usage in high-power applicants.

Targeting to solve this issue, it is essentially important to improve the diffusivity of lithium ions to achieve desirable electrochemical performance, in particularly high rate capability.[22] Tremendous efforts have been devoted to addressing this issue, among which the morphology design of hierarchical nano-/microarchitecture of NCM has been revealed as an effective solution.[23–28]

[a]*Key Laboratory of Engineering Dielectric and Applications (Ministry of Education), Harbin University of Science and Technology, Harbin 150080, P. R. China. E-mail: mhchen@hrbust.edu.cn*

[b]*Division of Physics and Applied Physics, School of Physical and Mathematical Sciences, Nanyang Technological University, 21 Nanyang Link, 637371, Singapore. E-mail: zexiang@ntu.edu.sg*

† Electronic supplementary information (ESI) available. See DOI: 10.1039/d0ra03022h

In our previous study,[25] we have already demonstrated that the diffusion length for Li^+ is effectively reduced through synthesizing hierarchical porous $LiNi_{1/3}Co_{1/3}Mn_{1/3}O_2$ with nano-/micro-architecture, in which the nano-sized primary particles contribute to excellent rate capacity while the micro-sized secondary particles stabilize the structure to ensure a good cycle life. The voids between the primary particles facilitate the penetration of electrolyte and thus allow for enhanced lithium ions diffusivity. Furthermore, the micro-sized secondary particles can increase the initial coulombic efficiency and are more suitable for commercial fabrication.[15]

Herein, we report an effective and efficient strategy to further boost the Li^+ diffusion ability *via* the synthesis of hierarchical porous $LiNi_{1/3}Co_{1/3}Mn_{1/3}O_2$ nano-/microspheres with yolk–shell-like architecture (hereafter denoted as YS-NCM). Besides of the above-mentioned advantages of the hierarchical nano-/micro-structure, the yolk–shell-like architecture of YS-NCM we designed here brings some additional benefits. The voids between the yolk and the shell can not only provide more buffers for the volume changes during repeated charge and discharge, but moreover enable more electrolyte penetration to further boost the Li^+ diffusions. Thereby, when revealed as the cathode material for lithium-ion batteries, the YS-NCM-based cells achieve superior capacity retention and excellent rate capability. Specifically, the capacity retention ratios as high as 85.99% (0.1C), 91.08% (1C) and 93.23% (2C) after 100 cycles have been achieved, respectively. In terms of the rate capability, the YS-NCM-based cells deliver discharge capacities of 145.93, 126.01, 109.58, 93.61, 79.16, 69.22 and 64.50 mA h g^{-1} at 1, 2, 5, 10, 15, 20 and 30C respectively. The design strategy presented in our work is expected to provide a useful idea for the synthesis of cathode materials with high long-term cycling stability and in particularly with high rate capability for lithium-ion batteries.

2. Experimental section

2.1 Preparation of $Ni_{1/3}Co_{1/3}Mn_{1/3}CO_3$ precursor

Firstly, stoichiometric amounts of $Ni(Ac)_2 \cdot 4H_2O$, $Co(Ac)_2 \cdot 4H_2O$ and $Mn(Ac)_2 \cdot 4H_2O$ were dissolved in ethylene glycol (40 mL) under rigorous stirring until a transparent solution was obtained. Then, 2.37 g of $(NH_4)HCO_3$ was added into the above solution which was kept under stirring till the salt was completely dissolved. In a next step, the mixed transparent solution was transferred into a Teflon-lined stainless steel autoclave with a volume of 50 mL, and then sealed tightly before transferred to an oven, in which the autoclave was quickly heated up to 200 °C and kept at such temperature for 20 h. The precursor product was collected and washed by centrifugation using deionized water (DIW) and absolute ethanol until the pH of the supernatant became neutral. The as-collected $Ni_{1/3}Co_{1/3}Mn_{1/3}CO_3$ was then dried in a vacuum oven at 80 °C overnight.

2.2 Preparation of $LiNi_{1/3}Co_{1/3}Mn_{1/3}O_2$ (YS-NCM)

The as-prepared $Ni_{1/3}Co_{1/3}Mn_{1/3}CO_3$ precursor was dispersed in ethanol (40 mL), together with $LiOH \cdot H_2O$ (6% excess to compensate the lithium evaporation during calcination and suppress the Li^+/Ni^{2+} cation mixing). The suspension was kept at 60 °C under continuous stirring overnight to get completely dried. The pre-dried powder was then collected and calcined in a tube furnace at 850 °C for 10 h in air atmosphere.

2.3 Material characterizations

X-ray diffraction (XRD) patterns were recorded using Bruker D8 with Cu Kα radiation ($\lambda = 0.15406$ nm). The thermal Brunauer–Emmett–Teller (BET) surface area and porosity were determined by nitrogen-sorption using a Micromeritics ASAP 2020 analyzer. Field-emission scanning electron microscopy (FESEM, JSM-7600F, JEOL) was used to investigate the morphology of both $Ni_{1/3}Co_{1/3}Mn_{1/3}CO_3$ and YS-NCM samples. Energy dispersive X-ray spectroscopy (EDS) (Oxford INCA, England) was used to characterize the elemental compositions of the YS-NCM sample. High resolution transmission electron microscope (HRTEM, JEOL JEM-2010F, 200 kV) was used to investigate the nanostructure of the $Ni_{1/3}Co_{1/3}Mn_{1/3}CO_3$ and YS-NCM samples.

2.4 Electrochemical measurements

All the electrochemical performance tests were carried out in CR2032 coin cells assembled in an argon-filled glove box (O_2 < 0.1 ppm, H_2O < 0.1 ppm) using metallic lithium as the counter electrode, Celgard 2400 films as the separator and 1 M $LiPF_6$ dissolved in ethyl carbonate–dimethyl carbonate (EC–DMC) (1 : 1 v/v) as the electrolyte. The electrodes were prepared by casting slurries (80 wt% of YS-NCM, 10 wt% of carbon black and 10 wt% of poly-(vinylidene fluoride) (PVDF) binder dissolved in *N*-methyl-2-pyrrolidone (NMP)) on aluminum foils using doctor blade technique. The wet electrodes were first pre-dried in an oven (60 °C, 1 h) and then vacuum dried in a vacuum chamber at 100 °C overnight. The average active material mass loading density of working electrodes is ~2.0 ± 0.2 mg cm^{-2}. All the electrochemical performance tests were conducted on a Neware battery tester. The cells were cycled in CCCV mode, and the termination condition of the constant voltage (CV) charging mode is the decreased current flow to one tenth of the given applied current. Cyclic voltammetry (CV) curves (five cycles at a scan rate of 0.1 mV s^{-1}) as well as the subsequent CV curves measured with increasing scan rates spanning from 0.1 mV s^{-1} to 1.5 mV s^{-1} were conducted on a CHI750d electrochemical workstation between the potential range of 2.5 and 4.5 V (*vs.* Li/Li$^+$). Electrochemical impedance spectroscopy (EIS) measurements were performed in two-electrode coin cells at room temperature with CHI760d electrochemical workstation over the frequency range between 0.1 Hz and 100 kHz.

3. Results and discussion

The synthesis route of the hierarchical porous yolk–shell-like $LiNi_{1/3}Co_{1/3}Mn_{1/3}O_2$ (YS-NCM) is illustrated in Fig. 1. The $Ni_{1/3}Co_{1/3}Mn_{1/3}CO_3$ microspheres, which were obtained *via* a hydrothermal method, serve as both the self-template and the precursor. After mixing homogeneously with $LiOH \cdot H_2O$, the powder mixture was then calcined in a tube furnace (850 °C for 10 h) to obtain the final product (YS-NCM).

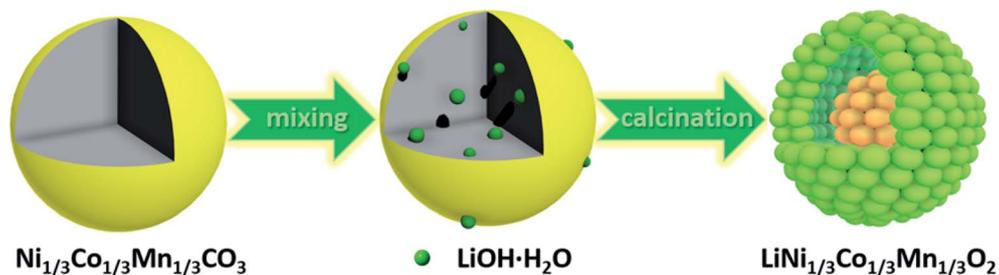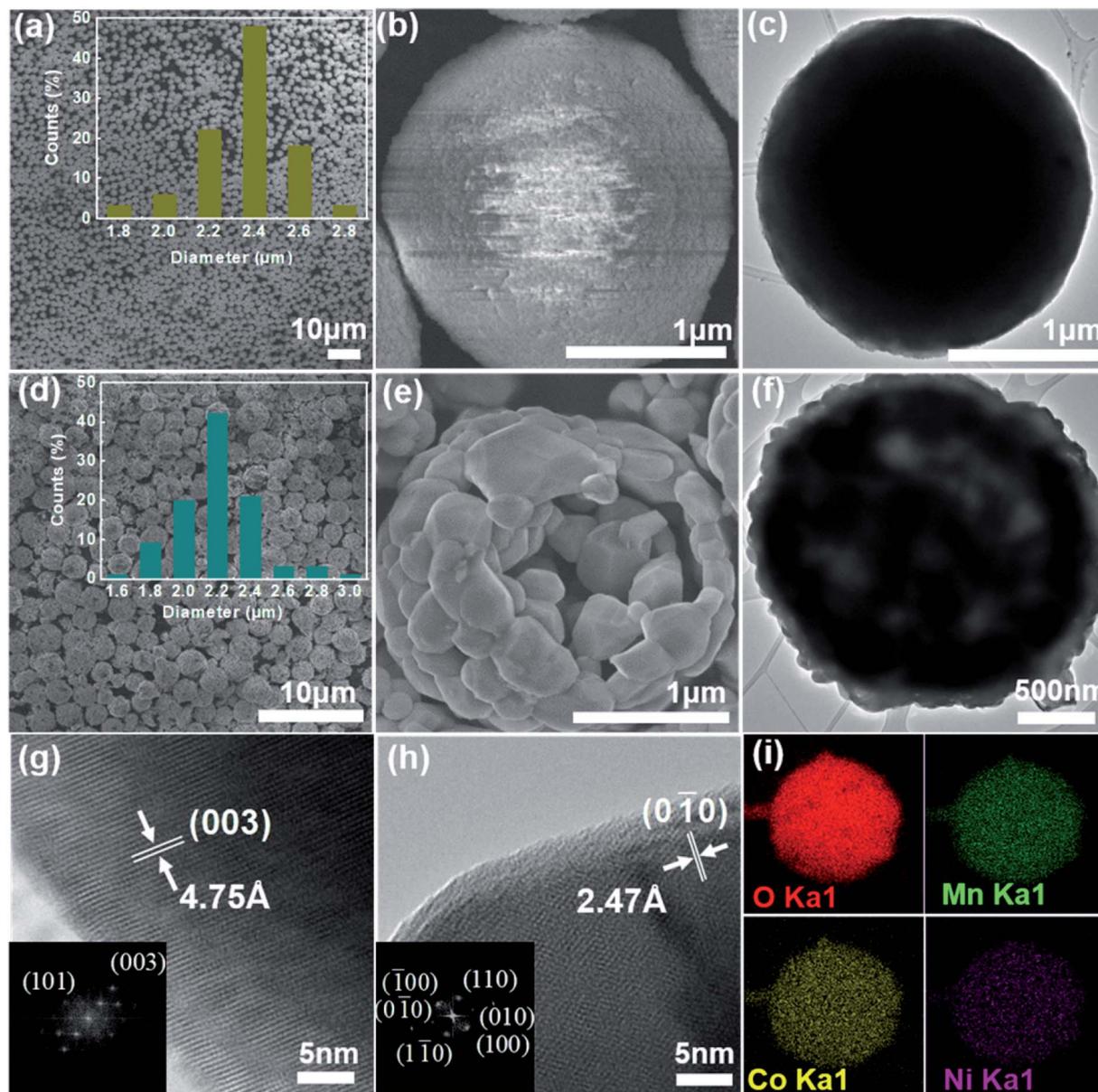**Fig. 1** Illustration of the synthesis route of YS-NCM.

Fig. 2 (a–c) Typical SEM and TEM images of $Ni_{1/3}Co_{1/3}Mn_{1/3}CO_3$ (inset: size distribution histograms derived from one hundred particles in (a)). (d–f) Typical SEM and TEM images of YS-NCM (inset: size distribution histograms gathered from one hundred particles in (d)). HRTEM images of (g) lateral plane and (h) frontal plane of YS-NCM (inset: fast Fourier transform (FFT) pattern). (i) EDS elemental mappings of YS-NCM.
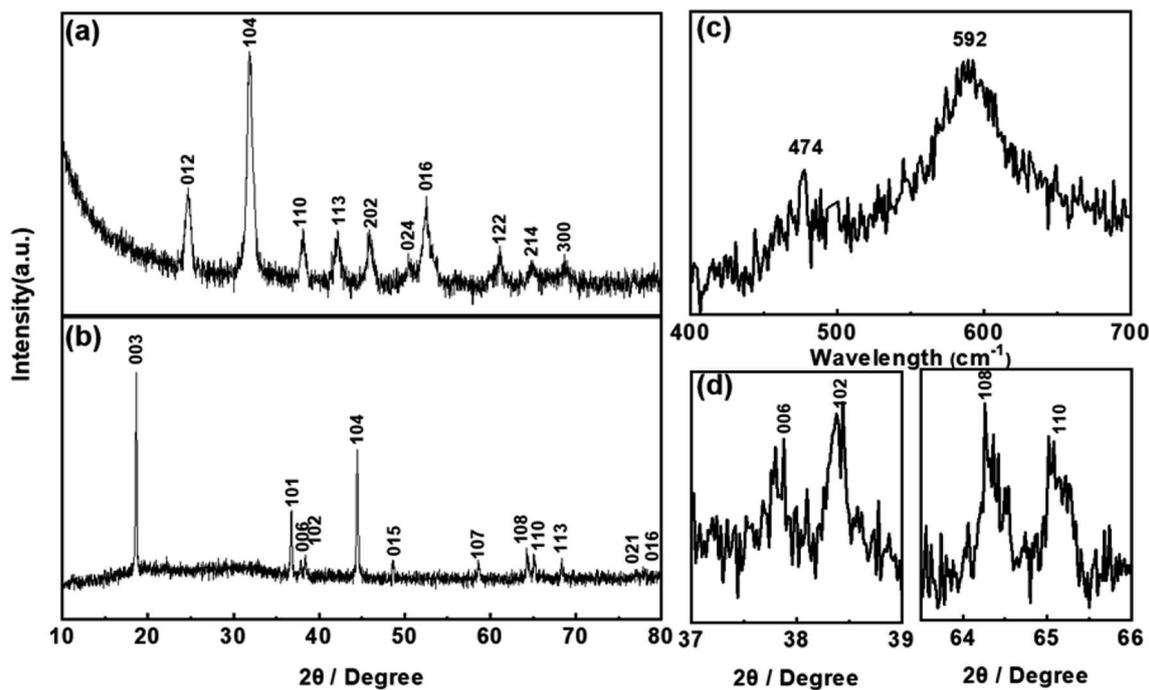
Fig. 3   XRD patterns of (a) $Ni_{1/3}Co_{1/3}Mn_{1/3}CO_3$, (b and d) YS-NCM. (c) Raman spectrum of YS-NCM.

The morphology of the $Ni_{1/3}Co_{1/3}Mn_{1/3}CO_3$ precursor at different magnifications is characterized by field-emission scanning electron microscopy (FESEM, Fig. 2a and b) and transmission electron microscopy (TEM, Fig. 2c). The mono-disperse feature of the precursor with spherical morphology is clearly revealed from the panoramic view (Fig. 2a). The average diameter of $Ni_{1/3}Co_{1/3}Mn_{1/3}CO_3$ microspheres is around 2.4 μm according to the statistical datum of one hundred particles (inset in Fig. 2a). The $Ni_{1/3}Co_{1/3}Mn_{1/3}CO_3$ microspheres are porous with a specific surface area of 73.24 m^2 g^{-1} (see ESI, inset in Fig. S1a†), determined by the nitrogen adsorption–desorption isotherm. According to the pore size distribution plot, the average pore size is ∼2 nm. The monodispersed porous $Ni_{1/3}Co_{1/3}Mn_{1/3}CO_3$ particles are favorable for the homogeneous mixing with Li^+ source and thus allow for a uniform solid state reaction during the subsequent calcination step.

From the panoramic view (Fig. 2d), it is obvious to see that the YS-NCM perfectly inherits the microspheres with rather intact morphology after calcination. The diameter of YS-NCM secondary particles, which are composed of many nano-sized primary particles, is around 2.2 μm (inset in Fig. 2d), slightly smaller than that of the precursor which can be due to the densification during calcination process. From our BET results (Fig. S1b†), the specific surface area of YS-NCM is 19.19 m^2 g^{-1}, which is at least comparable and even higher than those hier-archical porous structured $LiNi_{1/3}Co_{1/3}Mn_{1/3}O_2$.[29–31] According to the pore size distribution plot, two types of pore sized are observed, which are ∼1.2 nm and ∼2.5 nm, that could be resulted from the different densification level of the yolk and the shell parts during calcination step. A closer look of one representative broken microsphere of YS-NCM shown in Fig. 2e

reveals the yolk–shell-like structure of YS-NCM with hierar-chical nano-/micro-architecture. The thickness of the shell of YS-NCM is about 200 nm. Such a yolk–shell-like structure is further verified by a TEM image shown in Fig. 2f, in which the dark regions correspond to the yolk and shell parts with high thickness that blocks the transmission of electrons whereas the bright regions between the yolk and the shell correspond to the empty space. The formation of yolk–shell-like structure can be considered as a result of heterogeneous contraction caused by non-equilibrium heating.[32,33] Initially, a dense rigid shell is formed due to the large temperature gradient (ΔT) along the radical direction of the particles.[34] Between the dense shell and inner core there exist two forces, i.e. the cohesive force (σ_{co}) and the adhesive force (σ_{ad}) with opposite directions. The σ_{ad} force resists the inward shrinkage of the inner core while the σ_{co} causes the inner core shrinks inwards with occurrence of mass loss during heating. When $\sigma_{co} > \sigma_{ad}$, the inner core contracts inward and detaches from the dense shell, forming the yolk–shell-like structure eventually.

The high resolution TEM images and the corresponding fast Fourier transform (FFT) patterns (inset images) of the lateral plane and frontal plane of YS-NCM are shown in Fig. 2g and h, where two sets of clear lattice fringes are observed. One lattice fringe with an inter-planar spacing of 4.75 Å depicted in Fig. 2g corresponds to the (003) crystal plane of NCM, which indicates that the lateral plane is ($0\bar{1}0$) plane belonging to {010} active facet which provides unimpeded pathway for Li^+ insertion and extraction.[22,35] The other lattice fringe (Fig. 2h) can be assigned to ($0\bar{1}0$) plane with a lattice spacing of 2.47 Å. The FFT patterns indicate the single crystallinity of YS-NCM with a hexagonal symmetry, that is in consistence with a typical hexagonal

structure of NCM. The energy dispersive X-ray spectroscopy (EDS) mapping analysis was performed (Fig. 2i), showing the homogeneous elemental distributions of O, Mn, Co and Ni of YS-NCM. The molar ratio of Ni, Co and Mn is measured to be 1 : 1 : 1 (Fig. S2†), which is in a good agreement with the theoretical ratio.

The structural transformation process, *i.e.* from the precursor ($Ni_{1/3}Co_{1/3}Mn_{1/3}CO_3$) to final product ($LiNi_{1/3}Co_{1/3}Mn_{1/3}O_2$), is studied by X-ray power diffraction (XRD). The diffraction peaks presented in Fig. 3a can be indexed to a typical hexagonal structure with a space group of $R\bar{3}C$ corresponding to $MnCO_3$ (JCPDS no. 44-1472).[36] The diffraction pattern of YS-NCM displayed in Fig. 3b is

well assigned to the α-$NaFeO_2$ structure ($R\bar{3}m$ space group) without any impurity phase. Highly ordered hexagonal layered structure is discerned by the sharp reflections in the diffraction patterns with clear separations of the (006)/(102) and the (108)/(110) doublets (Fig. 3d). The peak intensity ratio of the (003) and (104) peaks is calculated to be 1.58 (>1.2), indicating a low Li^+/Ni^{2+} cation mixing. To further study the structure of YS-NCM, Raman spectroscopy, which is known to be quite sensitive in differentiating various structures of different atomic orderings, was carried out.[37,38] The Raman spectra of YS-NCM (Fig. 3c) show a broad band comprising of two bands at 474 and 592 cm^{-1}, assigning to the E_g (M–O–M bending) and the A_{1g} (M–O stretching) vibrations within
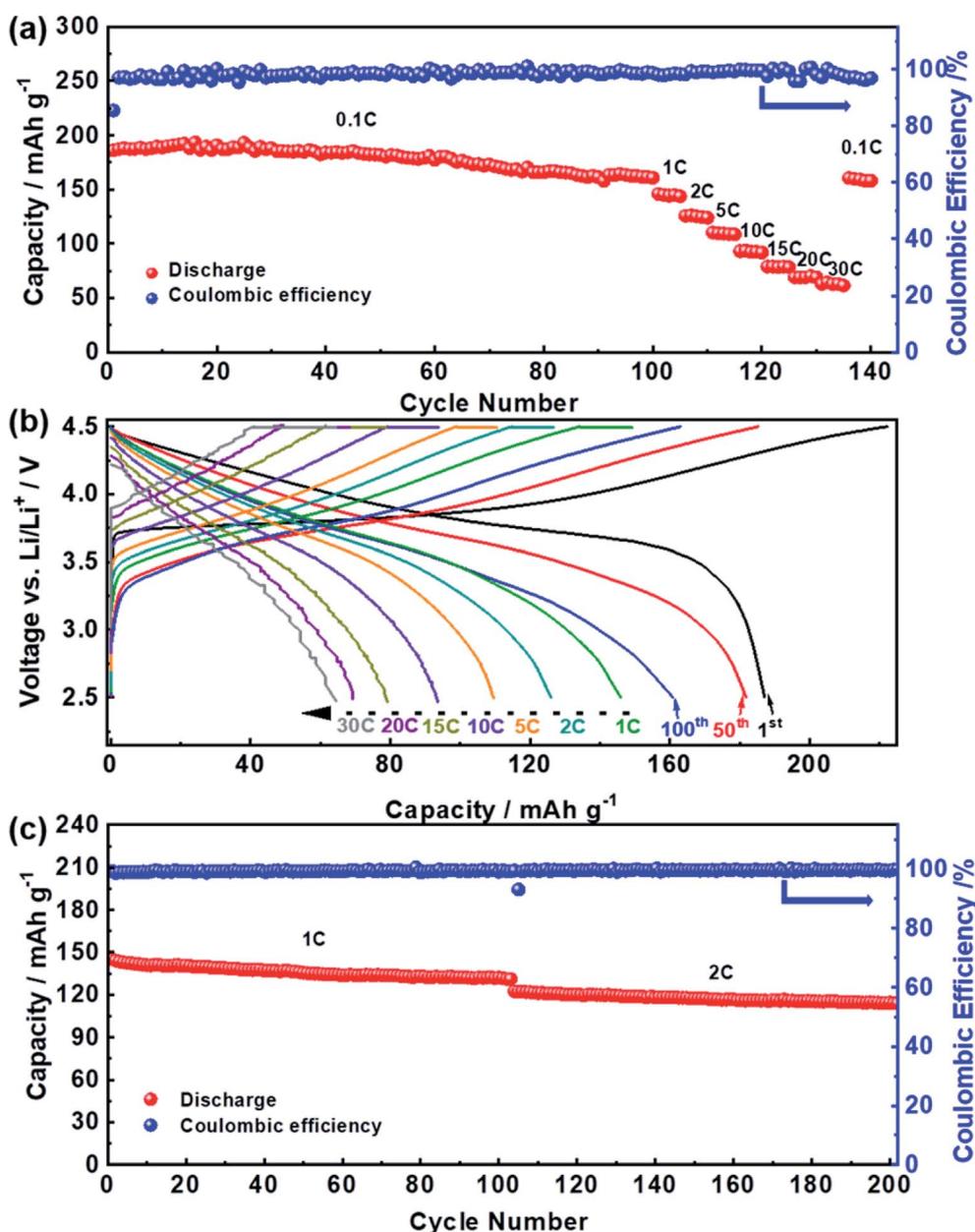

Fig. 4 Electrochemical performance investigation of the YS-NCM-based cells. (a) Cycling performance at 0.1C (100 cycles), followed by rate capability test at various C-rates. (b) Charge/discharge curves for selected cycles (1st, 50th and 100th) at 0.1C and charge/discharge profiles at various current rates from 1C to 30C. (c) Cycling performance at 1C (100 cycles) and 2C (100 cycles).

a hexagonal lattice belonging to the same space symmetry group ($R\bar{3}m$) respectively.[39–42]

The electrochemical performance of the YS-NCM-based cells is demonstrated in Fig. 4. A fresh cell was firstly subjected to a long-term cycling at 0.1C for 100 cycles, followed by a rate capability test at various C-rates (1C–30C, 1C = 200 mA g^{-1}, voltage range: 2.5–4.5 V). The initial charge and discharge capacities at 0.1C are 222.31 and 187.12 mA h g^{-1} respectively, yielding an initial coulombic efficiency of 84.17% (Fig. 4a). The cell can still deliver a capacity of 181.84 mA h g^{-1} after 50 cycles (97.18%) and 160.90 mA h g^{-1} after 100 cycles (85.99%). When subjecting to subsequent rate performance test at various C-rates (Fig. 4a), the YS-NCM-based cell can still retain reversible capacities of, *ca.*, 145.93 (1C), 126.01 (2C), 109.58 (5C), 93.61 (10C), 79.16 (15C), 69.22 (20C) and 64.50 (30C) mA h g^{-1}, respectively. Fig. 4b depicts some selected charge/discharge profiles of YS-NCM-based cell from Fig. 4a. It is notable that the initial charge/discharge profiles at a low C-rate of 0.1C are almost ideally symmetric, implying that kinetic difference upon charging and discharging is tiny. However, along with further consecutive cycling, these profiles become less symmetric, indicating higher polarization accumulates at discharge process. The long-term cycling performance at higher C-rates is revealed in Fig. 4c (after three formation cycles at 0.1C). The YS-NCM-based cells retain capacities of 132.13 mA h g^{-1} (1C) after 100 cycles and 114.11 mA h g^{-1} after another 100 cycles (2C), achieving capacity retention ratios of 91.08% (1C) and 93.23% (2C), respectively. All these results indicate that our YS-NCM-based cells exhibit superior long-term cycling stability and excellent high C-rates capability, which are at least comparable to or even better than the literature (see Table S1†). This is primarily owing to our design strategy that the hierarchical porous LiNi$_{1/3}$Co$_{1/3}$Mn$_{1/3}$O$_2$ nano-/microspheres with yolk–shell-like architecture and with exposed {010} active facets improve the Li$^+$ diffusion ability and meanwhile maintain the structure by providing sufficient buffers for volume changes upon charging/discharging.

To investigate the lithium lithiation/delithiation and charge-transfer kinetics, cyclic voltammetry (CV) and electrochemical impedance spectroscopy (EIS) measurements were performed as shown in Fig. 5. Fig. 5a depicts the cyclic voltammetry at increasing scan rates from 0.1 to 1.5 mV s^{-1}. According to Randles–Sevcik equation, the determination of lithium ion apparent diffusion coefficient can be achieved based on the plot of the peak intensity *versus* the square root of scan rates (derived from Fig. 5a).[43] The lithium ion diffusion coefficients are
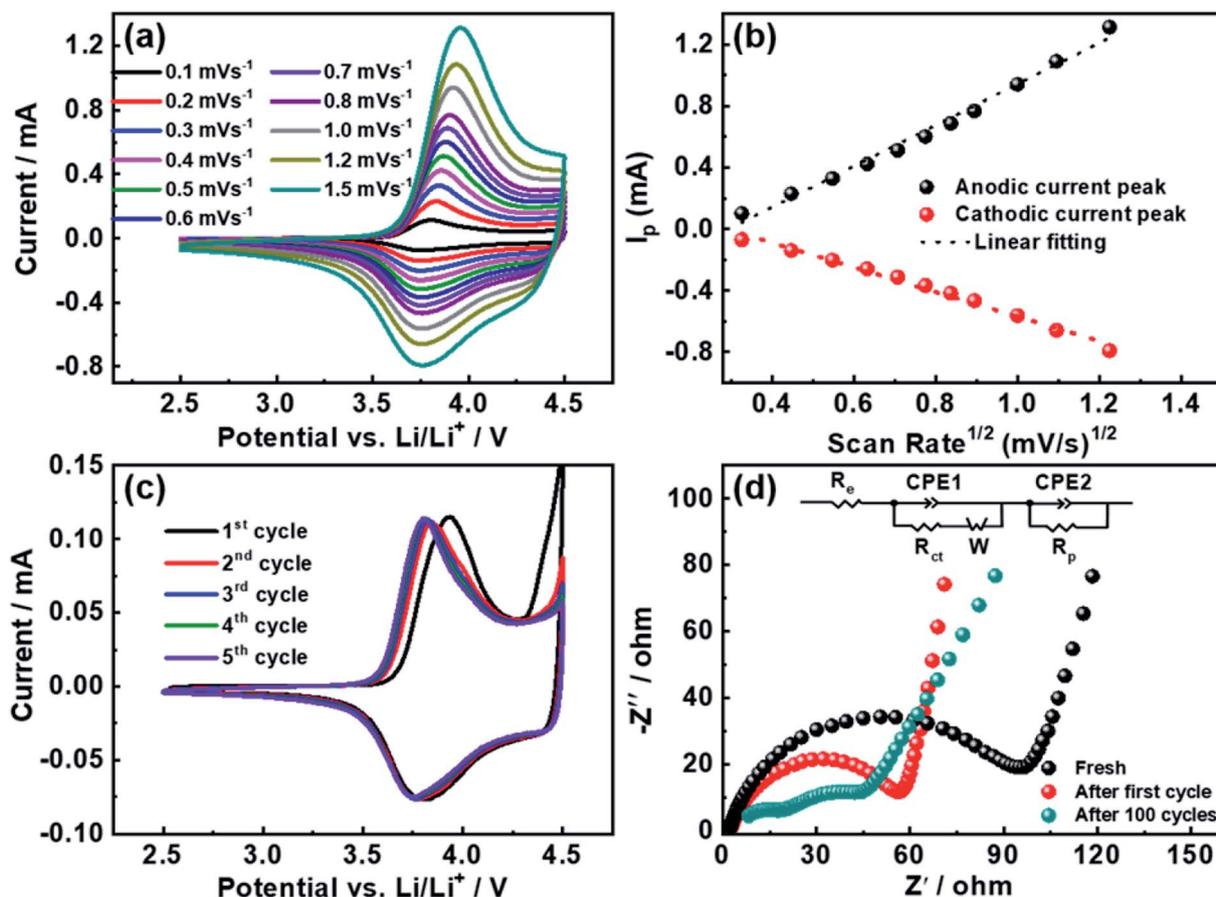

Fig. 5 Electrochemical behavior of YS-NCM-based cells. (a) Cyclic voltammetry profiles at various scan rates (0.1–1.5 mV s^{-1}). (b) Linear response of the peak current density as a function of the square root of scan rates. (c) Five consecutive cyclic voltammetry curves at a scan rate of 0.1 mV s^{-1}. (d) Nyquist plots of fresh cell as well as cell after different charge–discharge cycles over the frequency range from 0.1 Hz to 100 kHz.

calculated to be 4.5×10^{-9} and 1.6×10^{-9} cm^2 s^{-1} for delithiation and lithiation processes respectively, which is within the range of reported values.[16,25,30,44]

Fig. 5c shows the first five CV curves of YS-NCM swept in the voltage range of 2.5–4.5 V at 0.1 mV s^{-1}. A typical pair of redox peaks for NCM system was evidenced between 3.7 and 4.0 V with very small potential interval of the anodic and cathodic peaks, *ca.*, ~0.127 V for the initial cycle. For the following four cycles, the greatly reduced redox peak potential intervals and the perfectly overlapped curves suggest that the YS-NCM-based cell exhibits excellent reversibility and very small electrode polarization. Fig. 5d demonstrates the Nyquist plots (fresh, after one cycle, and after 100 cycles (0.1C)) of the YS-NCM-based cell, recorded over the frequency range from 0.1 Hz to 100 kHz. Typically, a depressed semicircle with a low-frequency oblique line is observed (Fig. 5d).[45] The intercept of the semicircle at high frequency region is related to the equivalent internal resistance (R_e), including a combination of total resistance from electrolyte, electrodes, separator. The semicircle in high-frequency region can be assigned to the resistance of the formation of a passivation layer (R_p) and the corresponding constant phase element (CPE). The middle-frequency semicircle is attributed to the charge transfer resistance (R_{ct}) together with its corresponding capacitance. The straight line in the low-frequency region is related to the Warburg diffusion process. After first electrochemical cycling, a greatly reduced R_{ct} and R_p is evidenced, primarily due to the reorganization of the lithium metal surface,[46] which usually takes a big share of the total resistance in half-cells. The YS-NCM-based cell shows even smaller resistance of R_{ct} and R_p after 100 cycles, implying that no severe resistance accumulation built upon cycling. Taken together the CV and EIS results, the fast Li$^+$ diffusion and charge transfer kinetics explain the superior C-rate capability and stable cycling performance we achieved here.

4. Conclusions

To sum up, in this work we designed and successfully synthesized the monodispersed hierarchical porous LiNi$_{1/3}$Co$_{1/3}$Mn$_{1/3}$O$_2$ nano-/microspheres with yolk–shell-like architecture (YS-NCM) and with exposed {010} electrochemical active facets. The morphology we designed here allows for fast Li$^+$ transport kinetics owing to both the shortened lithium-ion diffusion paths and the open structure of {010} facets. This is corroborated by the rather high lithium ion apparent diffusion coefficient derived from the cyclic voltammetry analysis. Furthermore, the yolk–shell-like structure is capable of buffering the volume changes upon charging/discharging. Benefiting from these, the YS-NCM-based cells demonstrate stable long-term cycling performance and outstanding high C-rates capability. Specifically, when examined as the cathode material for LIBs, the YS-NCM-based cells can maintain capacity retention ratios as high as 85.99% (0.1C), 91.08% (1C) and 93.23% (2C) after 100 cycles, respectively. Even being tested at 30C, our YS-NCM-based cells can still deliver a reversible capacity of 64.50 mA h g^{-1}, making our sample a highly promising candidate for practical lithium-ion battery applications with fast charge/discharge ability and superior long-term stability.

Conflicts of interest

There are no conflicts to declare.

Acknowledgements

Notes and references

1 J. M. Tarascon and M. Armand, *Nature*, 2001, **414**, 359–367.
2 M. S. Whittingham, *MRS Bull.*, 2008, **33**, 411–419.
3 B. Scrosati and J. Garche, *J. Power Sources*, 2010, **195**, 2419–2430.
4 V. Etacheri, R. Marom, R. Elazari, G. Salitra and D. Aurbach, *Energy Environ. Sci.*, 2001, **4**, 3243–3262.
5 R. Marom, S. F. Amalraj, N. Leifer, D. Jacob and D. Aurbach, *J. Mater. Chem.*, 2011, **21**, 9938–9954.
6 D. Bresser, K. Hosoi, D. Howell, H. Li, H. Zeisel, K. Amine and S. Passerini, *J. Power Sources*, 2018, **382**, 176–178.
7 T. Ohzuku and Y. Makimura, *Chem. Lett.*, 2001, **30**, 642–643.
8 N. Yabuuchi and T. Ohzuku, *J. Power Sources*, 2003, **119–121**, 171–174.
9 Y. Koyama, I. Tanaka, H. Adachi, Y. Makimura and T. Ohzuku, *J. Power Sources*, 2003, **119–121**, 644–648.
10 K. Dokko, M. Mohamedi, Y. Fujita, T. Itoh, M. Nishizawa, M. Umeda and I. Uchida, *J. Electrochem. Soc.*, 2001, **148**, A422–A426.
11 K. M. Shaju, G. V. Subba Rao and B. V. R. Chowdari, *Electrochim. Acta*, 2002, **48**, 145–151.
12 I. Belharouak, Y. K. Sun, J. Liu and K. Amine, *J. Power Sources*, 2003, **123**, 247–252.
13 K. M. Shaju and P. G. Bruce, *Adv. Mater.*, 2006, **18**, 2330–2334.
14 J. Zhu, T. Vo, D. Li, R. Lu, N. M. Kinsinger, L. Xiong, Y. Yan and D. Kisailus, *Cryst. Growth Des.*, 2012, **12**, 1118–1123.
15 J. Li, C. Cao, X. Xu, Y. Zhu and R. Yao, *J. Mater. Chem. A*, 2013, **1**, 11848–11852.
16 J. Li, S. Xiong, Y. Liu, Z. Ju and Y. Qian, *Nano Energy*, 2013, **2**, 1249–1260.
17 D. Becker, M. Börner, R. Nölle, M. Diehl, S. Klein, U. Rodehorst, R. Schmuch, M. Winter and T. Placke, *ACS Appl. Mater. Interfaces*, 2019, **11**, 18404–18414.
18 Z. Chen, G.-T. Kim, Y. Guang, D. Bresser, T. Diemant, Y. Huang, M. Copley, R. J. Behm, S. Passerini and Z. Shen, *J. Power Sources*, 2018, **402**, 263–271.
19 Z. Chen, D. Chao, J. Lin and Z. Shen, *Mater. Res. Bull.*, 2017, **96**, 491–502.
20 Y. Shao, B. Huang, Z. Lu, Y. Liu, X. Meng, L. Du, H. Song and S. Liao, *Energy Technol.*, 2019, **7**, 1800769–1800776.

21 M. Park, X. Zhang, M. Chung, G. B. Less and A. M. Sastry, *J. Power Sources*, 2010, **195**, 7904–7929.

22 Z. Chen, D. Chao, J. Liu, M. Copley, J. Lin, Z. Shen, G.-T. Kim and S. Passerini, *J. Mater. Chem. A*, 2017, **5**, 15669–15675.

23 B. Kang and G. Ceder, *Nature*, 2009, **458**, 190–193.

24 K. Kang, D. Morgan and G. Ceder, *Phys. Rev. B: Condens. Matter Mater. Phys.*, 2009, **79**, 014305–014308.

25 Z. Chen, J. Wang, D. Chao, T. Baikie, L. Bai, S. Chen, Y. Zhao, T. C. Sum, J. Lin and Z. Shen, *Sci. Rep.*, 2016, **6**, 25771–25781.

26 Z. Zhu, D. Zhang, H. Yan and W. Li, *J. Mater. Chem. A*, 2013, **1**, 5492–5496.

27 W. Xiong, Y. Jiang, Z. Yang, D. Li and Y. Huang, *J. Alloys Compd.*, 2014, **589**, 615–621.

28 Y. Wu, C. Cao, Y. Zhu, J. Li and L. Wang, *J. Mater. Chem. A*, 2015, **3**, 15523–15528.

29 J. Li, X. Wang, J. Zhao, J. Chen, T. Jia and C. Cao, *J. Power Sources*, 2016, **307**, 731–737.

30 L. Peng, Y. Zhu, U. Khakoo, D. Chen and G. Yu, *Nano Energy*, 2015, **17**, 36–42.

31 Z. Yang, J. Lu, D. Bian, W. Zhang, X. Yang, J. Xia, G. Chen, H. Gu and G. Ma, *J. Power Sources*, 2014, **272**, 144–151.

32 J. Guan, F. Mou, Z. Sun and W. Shi, *Chem. Commun.*, 2010, **46**, 6605–6607.

33 L. Zhou, D. Zhao and X. W. Lou, *Adv. Mater.*, 2012, **24**, 745–748.

34 F. Mou, J. Guan, Z. Sun, X. Fan and G. Tong, *J. Solid State Chem.*, 2010, **183**, 736–743.

35 N. Wu, Y. Zhang, Y. Guo, S. Liu, H. Liu and H. Wu, *ACS Appl. Mater. Interfaces*, 2016, **8**, 2723–2731.

36 Y. Jiang, Z. Yang, W. Luo, X. Hu and Y. Huang, *Phys. Chem. Chem. Phys.*, 2013, **15**, 2954–2960.

37 M. Delhaye and P. Dhamelincourt, *J. Raman Spectrosc.*, 1975, **3**, 33–43.

38 M. Delhaye, M. Bridoux and F. Wallart, *J. Mol. Struct.*, 1982, **79**, 51–66.

39 T. Mei, Y. Zhu, K. Tang and Y. Qian, *RSC Adv.*, 2012, **2**, 12886–12891.

40 C. Julien and M. Massot, *Solid State Ionics*, 2002, **148**, 53–59.

41 C. Julien, C. Letranchant, S. Rangan, M. Lemal, S. Ziolkiewicz, S. Castro-Garcia, L. El-Farh and M. Benkaddour, *Mater. Sci. Eng., B*, 2000, **76**, 145–155.

42 Z. Chen, Z. Wang, G.-T. Kim, G. Yang, H. Wang, X. Wang, Y. Huang, S. Passerini and Z. Shen, *ACS Appl. Mater. Interfaces*, 2019, **11**, 26994–27003.

43 Z. Chen, G.-T. Kim, D. Bresser, T. Diemant, J. Asenbauer, S. Jeong, M. Copley, R. J. Behm, J. Lin, Z. Shen and S. Passerini, *Adv. Energy Mater.*, 2018, **8**, 1801573–1801585.

44 B. Luo, B. Jiang, P. Peng, J. Huang, J. Chen, M. Li, L. Chu and Y. Li, *Electrochim. Acta*, 2019, **297**, 398–405.

45 K. M. Shaju, G. V. Subba Rao and B. V. R. Chowdari, *J. Electrochem. Soc.*, 2004, **151**, A1324–A1332.

46 G. B. Appetecchi, G.-T. Kim, M. Montanino, F. Alessandrini and S. Passerini, *J. Power Sources*, 2011, **19**, 6703–6709.